Monthly Notices of the ROYAL ASTRONOMICAL SOCIETY

MNRAS **501,** 36–49 (2021) doi:10.1093/mnras/staa3303
Advance Access publication 2020 October 29

AstroSat soft X-ray observations of the symbiotic recurrent nova V3890 Sgr during its 2019 outburst

K. P. Singh [1★] V. Girish,[2] M. Pavana [3,4] Jan-Uwe Ness,[5] G. C. Anupama[3★] and M. Orio[6,7]

[1]*Indian Institute of Science Education and Research Mohali, Sector 81, Manauli, SAS Nagar 140306, Punjab, India*
[2]*Indian Space Research Organisation HQ, Antariksh Bhavan, New BEL Road, Bengaluru 560094, Karnataka, India*
[3]*Indian Institute of Astrophysics, Koramangala, Bengaluru 560034, Karnataka, India*
[4]*Department of Physics, Pondicherry University, Puducherry 605014, India*
[5]*XMM–Newton Science Operations Center, ESAC, Camino Bajo del Castillo s/n, Urb. Villafranca del Castillo, E-28692 Villanueva de la Cañada, Madrid, Spain*
[6]*INAF – Osservatorio di Padova, Vicolo Osservatorio 5, I-35122 Padova, Italy*
[7]*Deptartment of Astronomy, University of Wisconsin, 475 N, Charter Street, Madison, WI 53706, USA*

Accepted 2020 October 21. Received 2020 October 21; in original form 2020 June 23

ABSTRACT

Two long *AstroSat* Soft X-ray Telescope observations were taken of the third recorded outburst of the symbiotic recurrent nova V3890 Sgr. The first observing run, 8.1–9.9 d after the outburst, initially showed a stable intensity level with a hard X-ray spectrum that we attribute to shocks between the nova ejecta and the pre-existing stellar companion. On day 8.57, the first, weak, signs appeared of supersoft source (SSS) emission powered by residual burning on the surface of the white dwarf. The SSS emission was observed to be highly variable on time-scales of hours. After day 8.9, the SSS component was more stable and brighter. In the second observing run, on days 15.9–19.6 after the outburst, the SSS component was even brighter but still highly variable. The SSS emission was observed to fade significantly during days 16.8–17.8 followed by re-brightening. Meanwhile, the shock component was stable, leading to increase in hardness ratio during the period of fading. *AstroSat* and *XMM–Newton* observations have been used to study the spectral properties of V3890 Sgr to draw quantitative conclusions even if their drawback is model dependent. We used the XSPEC to fit spectral models of plasma emission, and the best fits are consistent with the elemental abundances being lower during the second observing run compared to the first for spectra $\geq$1 keV. The SSS emission is well fitted by non-local thermal equilibrium model atmosphere used for white dwarfs. The resulting spectral parameters, however, are subject to systematic uncertainties such as completeness of atomic data.

Key words: stars: abundances – (stars:) novae, cataclysmic variables – X-rays: stars – novae: individual (V3890 Sgr).

1 INTRODUCTION

Novae are binary star systems wherein a white dwarf (WD) accretes matter from a donor that can be a main-sequence star or a red giant, as in some cases. The accreted material forms an accretion disc around the WD. Over a period of time, as the accreted material increases in mass, the temperature at the base of the accretion disc increases until explosive thermonuclear burning of the hydrogen-rich material ensues. The base of the accreted layer being electron degenerate leads to a thermonuclear runaway (TNR) condition and an eruption or an outburst that is observed as a nova (see Starrfield et al. 2012, for a review). The outburst also leads to ejection of the accreted material at velocities $\geq$300 km s^{-1} (e.g. Anupama & Kamath 2012). Novae with more than one recorded outburst are referred to as recurrent novae (RNe).

The critical mass needed to start a TNR is lower for a high-mass WD with high surface gravity. Therefore, RNe are expected to occur on WDs that are near the Chandrasekhar mass limit and accreting at a high rate, making them good candidates for being the progenitors of Type Ia supernova. This is one of the reasons for an intensive interest in the study of RNe. Readers are referred to comprehensive reviews of RNe by Schaefer (2010), Ness (2012), Anupama (2013), Mukai (2015), and Orio (2015).

Presently, there are only 10 confirmed RNe known in our Galaxy, making them very rare events (Schaefer 2010; Anupama 2013). Four of these are in binaries that contain a red giant mass donor, similar to symbiotic stars, and are sometimes also referred to as symbiotic RNe (Schaefer 2010). These are RS Oph, T CrB, V745 Sco, and V3890 Sgr. They all have an orbital period of the order of 1–2 yr (see Schaefer 2009). V3890 Sgr has an orbital period of 519.6 d and a recurrence time of $\sim$28 yr. The distance of V3890 Sgr has been found to be $4.36^{+2.64}_{-1.31}$ kpc from the *Gaia* DR2 parallax measurements (Bailer-Jones et al. 2018) with statistical error as given at the *Gaia* website.[1] The distance measurements to novae from *Gaia* have been discussed in detail by Schaefer (2018), who point out that these

★ E-mail: kpsinghx52@gmail.com (KPS); gca@iiap.res.in (GCA)

[1]gaia.ari.uni-heidelberg.de/tap.html

measurements can have large errors that will hopefully be improved in a later release of data.

The reddening measurement towards the nova obtained from the interstellar features in the optical spectra observed by Munari & Walter (2019) leads to $E(B-V) = 0.56$, which when compared with interstellar reddening maps indicates a distance of >4.5 kpc, which is within the uncertainty range of the *Gaia* distance. Here, we assume a distance of 4.4 kpc for V3890 Sgr.

V3890 Sgr went into eruption on 2019 August 27.87 (Pereira et al. 2019), and was immediately confirmed by Strader et al. (2019) through optical spectroscopy that showed very broad P Cygni profiles of H I and He I lines. Its two previous recorded outbursts were in 1962 (Duerbeck 1987) and 1990 (Jones & Pearce 1990; Liller 1990). Based on optical photometry, Sokolowsky et al. (2019) suggested that the nova peaked on 2019 August 28.1118 at $V = 7.17$ mag. The earliest emergence of X-rays was recorded on 2019 August 28.438 when a bright X-ray source at the position of the nova was reported by Sokolowsky et al. (2019) from observations with *Swift* Observatory (Burrows et al. 2005). An optical spectrum of V3890 Sgr obtained with the 2-m Himalayan Chandra Telescope on August 29 by Pavana, Anupama & Pramod Kumar (2019a) indicated the presence of weak coronal lines such as [Fe XIV] 5303 Å, [Ar X] 5535 Å, and [Fe X] 6374 Å. Strong coronal lines from the shock-heated plasma were detected during its 1990 outburst as well (Anupama & Sethi 1994). RNe with red giant secondary are known to exhibit a shock interaction of the nova ejecta with the red giant wind (Anupama & Mikolajewska 1998) giving rise to strong hard X-ray (and gamma-rays) and radio emission from the shock-heated plasma. Radio emission from V3890 Sgr was detected with the MeerKAT radio telescope (a precursor for the Square Kilometre Array) at 1.28 GHz by Nyamai et al. (2019) and with the Giant Metrewave Radio Telescope at 1.4 GHz and 610 MHz by Pavana et al. (2019b). Gamma-ray emission was also detected by the Large Area Telescope on the *Fermi* Gamma-ray Space Telescope, during 2019 August 26–29 (Buson, Jean & Cheung 2019).

Soft X-rays in symbiotic RNe are believed to arise predominantly from matter shocked and heated by the nova blast wave from the surface of the WD interacting with the wind from the red giant donor. The shock-heated ejecta from these novae evolve extremely rapidly during the outbursts and require almost continuous monitoring. In the recent outburst from V3890 Sgr, Orio et al. (2020) reported a rich emission-line spectrum in X-rays from their observations in the 1.2–15 Å range with the *Chandra* Advanced CCD Imaging Spectrometer - Spectroscopic (ACIS-S) camera and high-energy transmission gratings (HETGs) on 2019 September 3 (starting on day 6.4 since the onset of the optical outburst). The high-resolution X-ray spectra revealed several prominent features due to transitions in Fe-L and K-shell ions ranging from neon to iron. A couple of days later, Page et al. (2019a) reported a decrease in the absorption in V3890 Sgr and emergence of supersoft phase around day 8.57 from their observations with *Swift* Observatory. The origin of the supersoft source (SSS) is the residual burning on the surface of the WD (e.g. Krautter 2008). A deep, continuous, *XMM–Newton* observation during the SSS phase was described by Ness et al. (2019). The high-resolution spectrum taken with the reflection grating spectrometer (RGS) is dominated by several absorption edges and emission lines along with plasma emission and a blackbody continuum with an effective temperature of 6×10^5 K. Several deep absorption lines, most prominently of H-like and He-like nitrogen and oxygen, are measured with the RGS. A deep dip in the middle of the RGS observation seems to have brought the overall spectrum back to the pre-SSS status, suggesting a complete obscuration of all SSS emission.

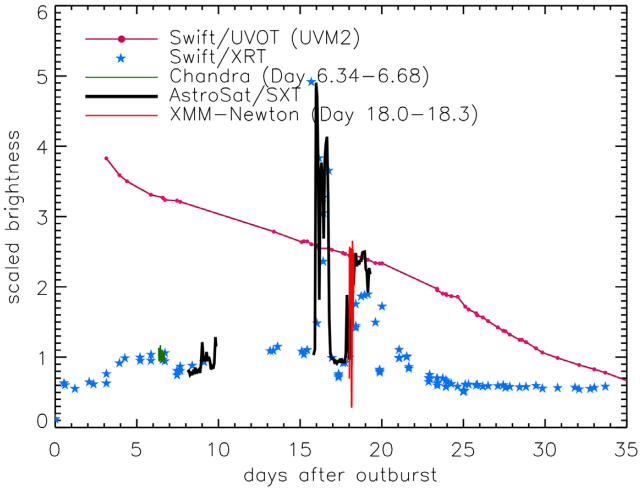

Figure 1. The X-ray (0.5–10.0 keV) and optical light curve of V3890 Sgr as obtained with *Swift* XRT and Ultraviolet/Optical Telescope (UVOT). The *AstroSat* observations (0.3–7.0 keV) are shown superimposed in black. Also shown are the light curves taken with *Chandra*/ACIS (zero order, ObsID 22845) and *XMM–Newton*/MOS2 (ObsID 0821560201).

India's first multiwavelength space observatory *AstroSat* (Singh et al. 2014) observed V3890 Sgr twice, with its three co-aligned X-ray instruments, namely the Soft X-ray Telescope (SXT), Large Area Xenon Proportional Counters, and Cadmium Zinc Telluride Imager. The main instrument used for these observations was SXT (Singh et al. 2016, 2017). The timing and duration of the *AstroSat* observations are shown in Fig. 1 to put them in perspective with the regular monitoring carried out by the *Swift*. The *AstroSat* observations were long and carried out with the densest possible monitoring of V3890 Sgr with a satellite in near-Earth orbit. The first observation saw the emergence of the SSS phase in V3890 Sgr accompanied by strong variability (Singh et al. 2019a). Large amplitude and rapid variability during the SSS phase were confirmed with *Swift* observations by Beardmore et al. (2019). The SSS phase ended by day 26.2 as reported by Page et al. (2019b). In the meanwhile, *AstroSat* SXT had a second long observation of the source during the SSS phase from days 15.9 to 19.6 since the outburst (Singh et al. 2019b). The second observation coincided with the peak intensity of the outburst detected with the *Swift* X-ray Telescope (XRT). Dips in the XRT light curve are detected around days 7–8, days 17–18, and day 20. *AstroSat* observations provided us with an opportunity to study complex intensity and spectral evolution in soft X-rays – the quick emergence of the SSS phase, and the rapid variability on time-scales of minutes to hours.

In this paper, we present a detailed spectral analysis of X-ray emission observed with the *AstroSat* SXT on two extended epochs during the recent outburst of V3890 Sgr, and its spectral evolution. In Section 2, we describe our SXT observations, and also part of near-simultaneous observation with *XMM–Newton*, used for comparison purposes. Section 3 contains the analysis of the X-ray light curves and spectra. Results obtained from fitting non-local thermal equilibrium (NLTE) atmosphere models used for WDs and thin plasma emission models for shocked ejecta are described here. In Section 4, we discuss our results and compare them with other similar systems, and finally we present our conclusions in Section 5. The results of our monitoring in the optical and radio will be presented in an accompanying paper (M. Pavana et al., in preparation).

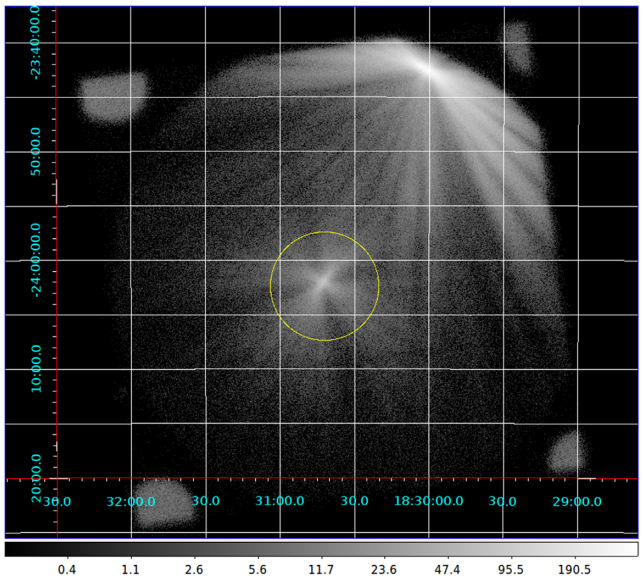

Figure 2. Soft X-ray image of V3890Sgr in the energy range of 0.3–7.0 keV taken during the second epoch of observations with the *AstroSat* SXT. Full field of view of the SXT is shown. Log scale is used to show the full dynamic range of brightness. A circle with a radius of 5 arcmin used to extract spectra and light curve is shown. The four bright spots on the corners are the calibration sources.

2 OBSERVATIONS AND DATA REDUCTION

2.1 *AstroSat*

V3890 Sgr was observed with the *AstroSat* via a proposal submitted under the Target of Opportunity programme (observation IDs: 9000003142 and 9000003160, PI: V. Girish) with SXT configured as the prime instrument. V3890 Sgr was observed throughout an orbit of the satellite while taking care that the Sun avoidance angle was $\geq 45^\circ$ and ram angle (the angle between the payload axis and the velocity vector direction of the spacecraft) $>12^\circ$ to ensure the safety of the mirrors and the detector. The first observation (ID 9000003142, hereafter S1) was started on 2019 September 5 at 01h:37m:55s UT and ended on 2019 September 6 at 20h:19m:27s UT, thus covering the days 8.198–9.977 after the outburst. The second observation (ID 9000003160, hereafter S2) was from 2019 September 12 at 18h:45m:95s UT to 2019 September 16 at 07h:14m:32s UT, thus extending from days 15.9 to 19.6 after the outburst (see Fig. 1 and Section 1). The two observations are not continuous but consist of segments collected during an *AstroSat* orbit, which are shorter than the orbit due to various observational constraints mentioned above and further data filtering that follows.

Data from individual orbits of the satellite (level-1 data) were received at the SXT Payload Operation Centre (POC) from the Indian Space Science Data Center (ISSDC). The level-1 SXT data obtained in the photon counting mode were first processed with the *sxtpipeline* task available as part of the SXT software (AS1SXTLEVEL2, version 1.4b) at the SXT POC website.[2] The pipeline calibrates the source events and extracts level-2 cleaned event files for the individual orbits. The clean process filtered out any contamination by the charged particles due to excursions of the satellite through the South Atlantic Anomaly region and occultation by the Earth, and selected only the events with grade 0–12 (single-quadrupal events) representing only X-rays and eliminating charged particles (Burrows et al. 2005). The cleaned event files of all the orbits were then also merged into a single cleaned event file using Julia-based merger tool developed by G. C. Dewangan to avoid any time-overlapping events from the consecutive orbits. The XSELECT (V2.4d) package built-in HEASOFT[3] was used to extract the source spectra and light curves from the processed level-2 cleaned event files – merged as well as orbit-wise files. Therefore, useful exposure times in each orbit of *AstroSat* are shorter than its orbit and vary from ∼300 to ∼3000 s. Total useful exposures obtained are 39 894 and 65 844 s for the merged data from S1 and S2 observations, respectively. A full-field X-ray image from an observation targeting V3890 Sgr taken with the SXT in the energy band of 0.3–7.0 keV is shown in Fig. 2. A bright source, GS 1826−238, which is 21.7 arcmin away (towards the top right of Fig. 1), is observed at the very edge of the field of view. Care was taken to minimize the contamination due to scattered X-rays from GS 1826−238 by restricting the extraction of X-ray events from V3890 Sgr to a circle of radius 5 arcmin for light curves and spectra presented in the next section. Since the point spread function (PSF) of images formed in the SXT is large (full width at half-maximum of ∼2 arcmin and half-power width of 10 arcmin) due to scattering by the mirrors and attitude control of the satellite (Singh et al. 2016), the extraction is typically carried out for a radius of 10–14 arcmin, depending on the brightness of the source. Based on the radial profiles derived for V3890 Sgr and GS 1826−238 and the PSF measurements (Singh et al. 2016), we estimated that in our circle of extraction (Fig. 2) the contamination due to GS 1826−238 is ∼2–4 per cent for soft X-rays (<2 keV) and ∼10–12 per cent for hard X-rays (2–7 keV), depending on the intensity of V3890 Sgr.

2.2 *XMM–Newton*

XMM–Newton (Jansen et al. 2001) observed V3890 Sgr on 2019 September 14, during the second observing run with SXT. The *XMM–Newton* observation under ObsID 0821560201 is part of a larger data set that is being processed for publication in a forthcoming paper (Ness et al., in preparation) and here only a subset of the data is used for comparison. We use here the MOS2 observation that was taken in timing window mode with the thin optical blocking filter for purposes of comparison with SXT spectra. The observation lasted from 2019 September 14 23h:48m:22s UT to 2019 September 15 06h:21m:24s UT for useful exposure time of 23.4 ks. We extracted light curve and spectrum using the *XMM–Newton* Science Analysis Software (SAS) version 17.0.0. For both light curve and spectrum, we filtered on the same RAWX columns 305–319 in the detector pixel coordinates, and the background was extracted from RAWX columns 260–270. The raw light curve was then corrected with the EPICLCCORR task in SAS. It contains a deep dip shown in Fig. 1 (Ness et al. 2019) that we have excluded when extracting the MOS2 (and MOS1 – see below) spectrum by filtering on the timestamp ranges (6.848 9253–6.849 0220) $\times 10^8$ and (6.849 0711–6.849 1643) $\times 10^8$ s (19 ks). The pixel coordinates above and the timestamps are given to reproduce the results and have been determined by eye. In addition to source and background spectra, we extracted the detector responses with the RMFGEN task and the effective area file with ARFGEN. We also extracted the spectrum from the MOS1 detector that was operated in small window mode with a thin optical blocking filter. The observation lasted from 2019 September 14 23h:48m:06s

[2]https://www.tifr.res.in/~astrosat_sxt/sxtpipeline.html

[3]https://heasarc.gsfc.nasa.gov/docs/software/lheasoft/

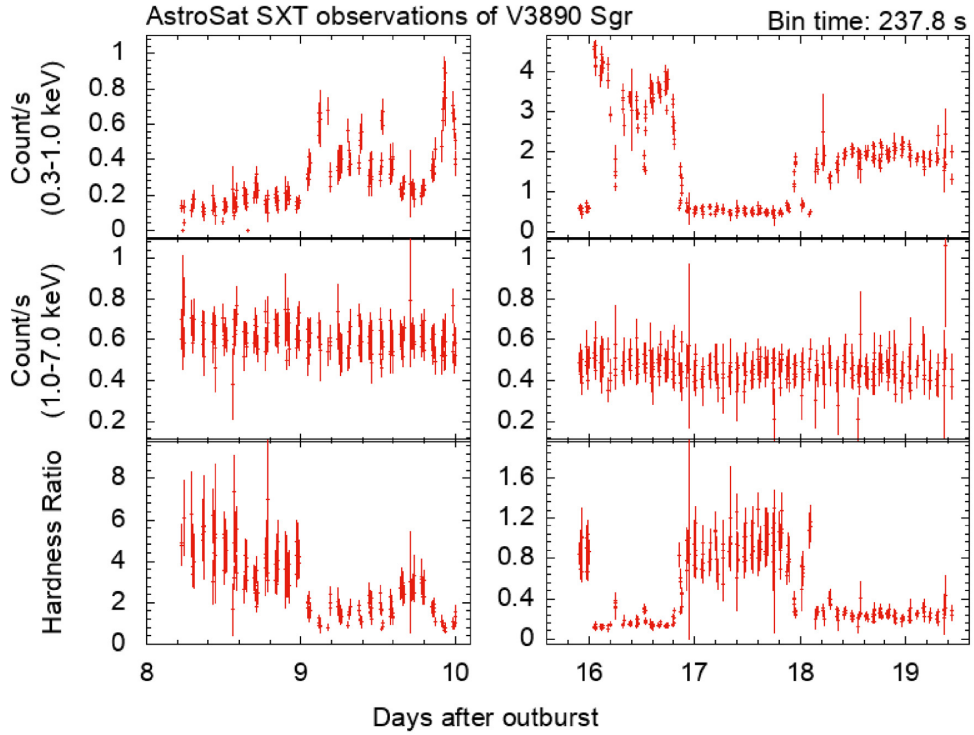

Figure 3. X-ray light curves and hardness ratios of V3890 Sgr for both S1 (left-hand panels) and S2 (right-hand panels) observations. The top panels show the light curves in the soft energy band of 0.3–1.0 keV. The middle panels show the light curves in the energy range of 1.0–7.0 keV. The bottom panels show the hardness ratio as described in the text. The *X*-axis refers to the days after the outburst. Please note that the *y*-axis scales are different for the top and bottom panels for the S1 and S2 observations.

UT to 2019 September 15 06h:25m:33s UT for useful exposure time of 23.6 ks. Owing to the longer readout time, the spectrum is heavily piled up and could only be brought down by excluding the central 250 pixels. The source extraction region was located at (27 045, 27 598) detector pixels with an outer extraction radius of 400 pixels. The background spectrum was extracted from pixel position (28 053, 26 574) with a radius of 180 pixels, somewhat smaller than the source region to avoid source photons to fall into the background extraction region while still fitting into the small window mode.

3 ANALYSIS AND RESULTS

3.1 X-ray light curves

SXT light curves of V3890 Sgr extracted from the two observations S1 and S2 are shown in Fig. 3 for two energy bands: soft band of 0.3–1.0 keV (top panels) and hard band of 1.0–7.0 keV (middle panels). The data were binned in time bins of 237.8 s. These light curves show that (a) the count rates in the soft band are highly variable, (b) the average count rates during S1 observation are more in the high-energy band than those in the softer band, and (c) the intensity in the hard energy band is considerably weakened vis-a-vis the softer energy band in the S2 observations. The overall trends in the hard band count rates are also reflected in the hardness ratios plotted in the bottom panels of Fig. 3, where the hardness ratio is defined as the ratio of count rates in the hard band divided by the count rates in the soft band. The count rates in the hard band, however, appear to be nearly constant with a count rate of 0.607 ± 0.004 for the S1, and 0.456 ± 0.003 for the S2 observations. The variance seen around the constant value is 231.5 for 199 data points in S1 data, and 346.5 for 337 data points. Light curves shown are not background subtracted. The same observation cannot be used for extracting the background for the observation for the reasons of PSF mentioned in the previous section. The background in SXT used here is estimated from deep observations of source-free regions at mid-Galactic latitudes (32° and −32°) and is found to be very steady at 0.012 ± 0.005 count s^{-1} in the soft band and 0.014 ± 0.005 count s^{-1} in the hard band, in this nearly equatorial and low-Earth orbit satellite after the usual screening of events described in the previous section and for the same extraction radius as used for V3890 Sgr. Thus, the background is almost negligible here compared to the count rate registered from V3890 Sgr. The hardness ratio variations observed (Fig. 3) appear to be in anticorrelation with the variations seen in the soft band.

Short-term variability was detected in the soft band (<1 keV) emission, as already reported in Singh et al. (2019a). These rapid variations were further studied by creating light curves with shorter time bins of 35.6625 s. Some examples of rapid (minutes to hours time-scales) variability are shown in Fig. 4. These variations are seen to be mostly sporadic and random and are difficult to characterize with any particular mathematical form or structure, like flares, etc.

The light curves were also extracted with the highest available time resolution of 2.3775 s in the SXT for period search in the soft band, the hard band, and total energy band of 0.3–7.0 keV. The light curves were first subjected to fast Fourier transform using the *powspec* tool from the XRONOS package in HEASOFT version 6.20. As the SXT light curves are not continuous but have several gaps due to *AstroSat*'s low-Earth orbit, the output power spectra from *powspec* has many false peaks. To search for real periods, these periodograms were passed through the *clean* algorithm by (Hoegbom 1974; Roberts et al. 1987) as implemented in Interactive Data Language by Fullerton et al. (1997) using a low gain of 0.001 and passing through 30 000 iterations. The high-energy data

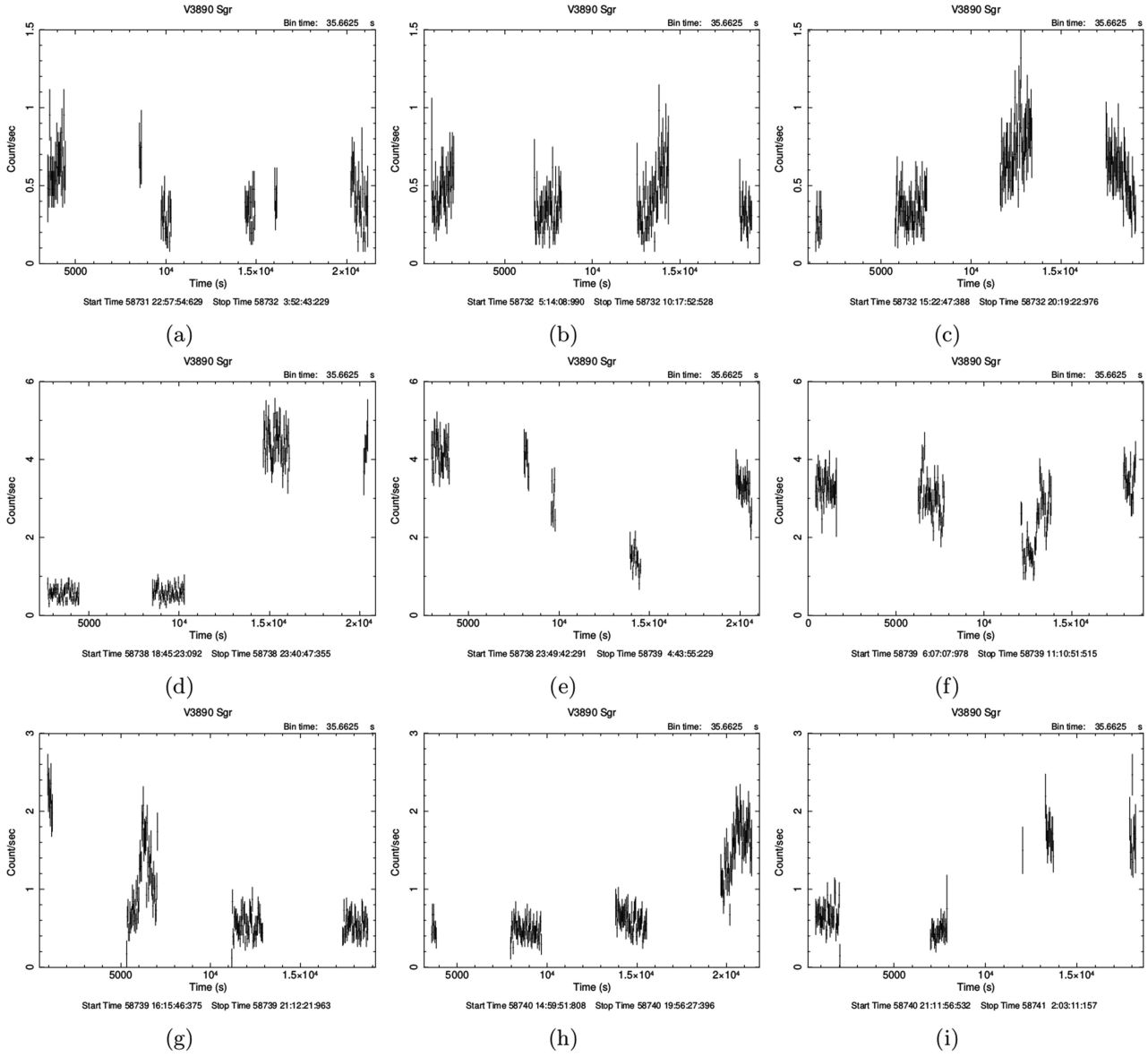

Figure 4. Examples of high time resolution variability in the soft energy band of 0.3–1.0 keV from the S1 observations (panels a–c), and from S2 observations (panels d–i). The times shown here are in units of seconds and the duration shown is in MJD: Mean Julian Day. For reference, the start time, t_0, of nova is MJD 58722.87. The *y*-axis scale has been chosen to be different to show the range and details of variations, appropriately.

(>1.0 keV) do not show any significant periodicity. Multiple peaks common to both S1 and S2 observations were detected in the power spectrum of the low-energy (<1 keV) data corresponding to 0.56 d, 1.67 h, and 1.59 h. These seem to be related to the observation duration and orbital period of *AstroSat* and, therefore, are not related to the source.

3.2 X-ray spectra

X-ray spectra were extracted for the duration of each orbit of *AstroSat* amounting to 28 spectra in observation S1, and 51 spectra during S2, to understand the variability seen in V3890 Sgr over time-scales of hours. All the individual spectra derived from the duration of each orbit of the satellite for the S1 observation and S2 observation are shown in Figs 5 and 6, respectively. These figures reiterate that almost all the spectral variability is confined to the soft energy bands (as was also depicted in Fig. 3). A clear increase in the flux for energies below 0.8 keV, coincident with the onset of the SSS phase around day 8.57 after the outburst (see Section 1), can be seen in S1 observations shown in Fig. 5. This figure also shows that the flux above 0.8 keV is almost constant and that the variability is confined to energies below 0.8 keV, thus marking a natural boundary between the variable low-energy spectral hump and the nearly constant emission above that energy. The delineation in energy between the variable intensity portion and the constant intensity portion is not as clear in the case of S2 observation (Fig. 6), however. In the case of S2 observations, the variable parts of the spectra show a double hump extending in energies to ∼1.1 keV, and the nearly constant intensity part (third hump) begins only at energies greater than ∼1.1 keV. Since the flux at higher energies (>0.8 keV for S1 and >1.1 keV for S2) is nearly constant during each orbit of the observation, though varying from S1 to S2 observations separated by ∼6 d, we also derived two merged

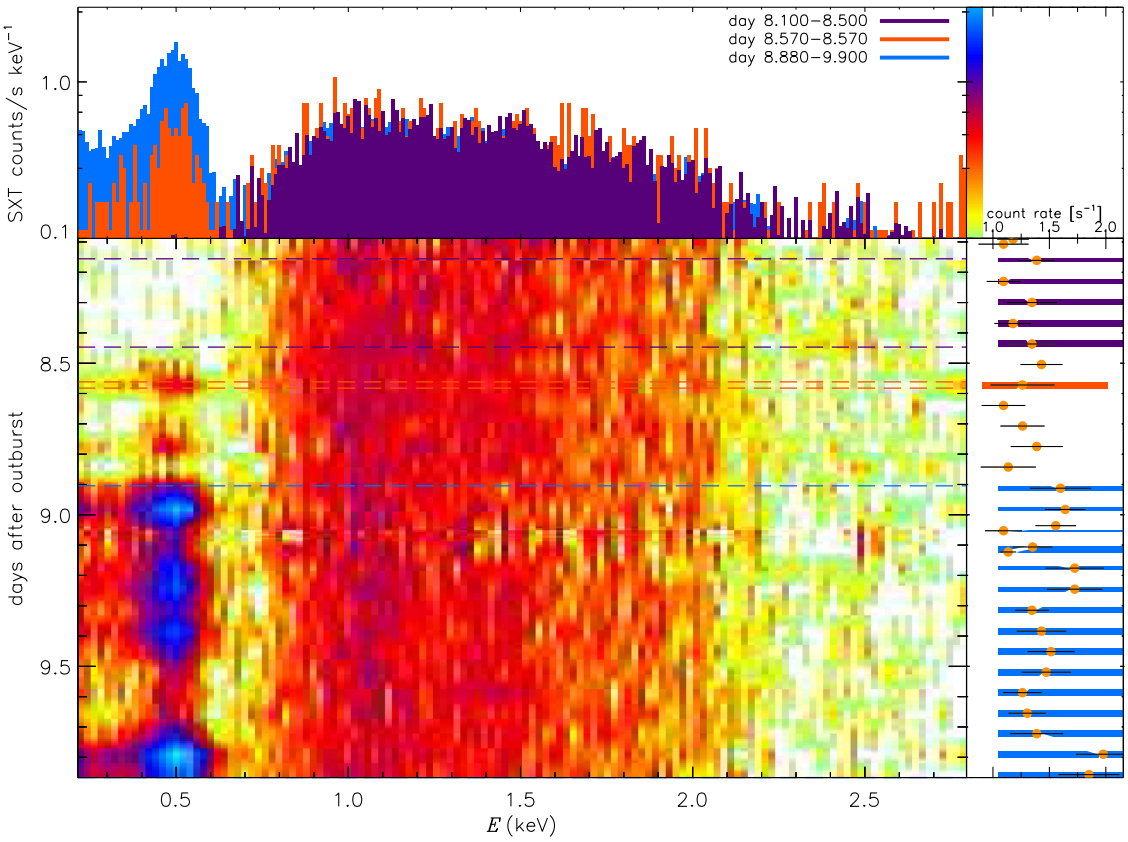

Figure 5. Spectral evolution map from the observation S1 with the *AstroSat* SXT. The top panel displays spectra extracted from time intervals corresponding to the horizontal dashed lines of the same colours in the time map below and in the light curve to the right (rotated by 90°). The central panel shows the spectral time evolution with elapsed observing time along the vertical axis and photon energy on the horizontal axis, on the same scales as the light curve in the right and the spectra on top, respectively. The brightness is colour coded, and for each colour, the corresponding count rate can be derived from the colour bar in the top right. (Correction: day 8.570-8.570 should read as day 8.570-8.880).

X-ray spectra – one using all the data from the S1 observations, and another using all the data from the S2 observations, thus creating two spectra with long exposures for the study of weak hard X-ray emission part of the spectrum that hardly varies. The two SXT spectra with long exposures, S1 and S2, are shown in Fig. 7. Because these hard portions of X-ray spectra vary from S1 to S2 (see Section 3.1), we modelled these X-ray spectra separately. The lower limit for the energy used for spectral analysis of the non-variable component was 0.8 keV for the S1 observation and 1.1 keV for the S2 observation, thus avoiding the variable softer component completely in S1 and to a large extent in S2. Modelling the steady high-energy part of these two spectra with high signal-to-noise ratio allowed us to freeze the model parameters for the steady part, thus enabling the study of the highly variable low-energy spectra from each of the orbits (with short exposures and low signal-to-noise ratio) by varying only a few parameters (see Section 3.2.1 below). This also enabled us to compare the SXT data with contemporaneous *Chandra* and *XMM–Newton* observations (see below).

The spectra were modelled using the XSPEC program (version 12.9.1; Arnaud 1996) distributed with the HEASOFT package (version 6.20). A background spectral file 'SkyBkg_comb_EL3p5_Cl_Rd16p0_v01.pha', derived from a composite of several deep sky observations of source-free regions taken from mid-Galactic latitudes (see Section 3.1), and distributed by the instrument team, is used in the analysis of all the spectra analysed here. We used the ancillary response file 'sxt_pc_excl00_v04_20190608.arf'. Similarly, the spectral response file used in this work is sxt_pc_mat_g0to12.rmf. The spectral and ancillary responses and the background files are available at the SXT POC website (see Section 2).[4] The counts in the spectra were grouped using the *grppha* tool to ensure a minimum of 25 counts per bin, prior to further analysis here and below. We used χ^2 statistic to assess the goodness of the fit.

Following the modelling of the *Chandra* HETG spectra by Orio et al. (2020), where the intensity level was about the same as in the case of our S1 observation that was carried out ∼2 d after the *Chandra* observation (see Fig. 1), the merged hard S1 spectrum (with about the same energy band as in HETG spectra) shown in the left-hand panel of Fig. 7 was modelled by fitting a two-component thin thermal plasma in collisional ionization equilibrium. This plasma model, known as *bapec* (Broadened Astrophysical Plasma Emission Code) in XSPEC, calculates emission spectrum from collisionally ionized diffuse gas using the AtomDB atomic data base (version 3.0.7)[5] incorporating velocity and thermal broadening. We used the line shifts and line broadening values reported by Orio et al. (2020) as fixed parameters, while the temperatures of the two *bapec* models were kept as free parameters. The specific values of the line blueshifts and thermal velocities were: $z = -0.002\ 89$ and $v =$

[4] https://www.tifr.res.in/~astrosat_sxt/index.html
[5] http:///www.atomdb.org/index.php

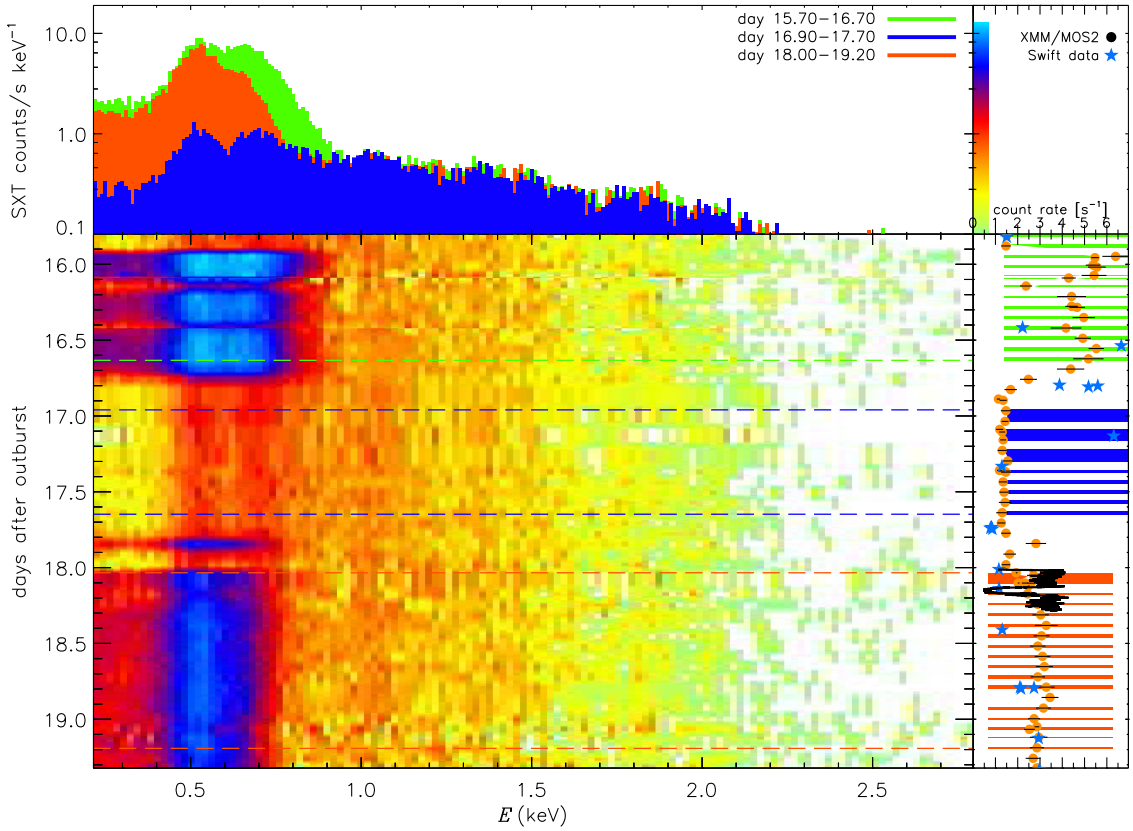

Figure 6. Same as in the Fig. 5 but for the S2 observation with the *AstroSat* SXT. Also shown on the right-hand panel, at 90°, are scaled counts from near-simultaneous measurements with *Swift* XRT (blue stars) and *XMM–Newton* (black line, Ness et al. 2019).

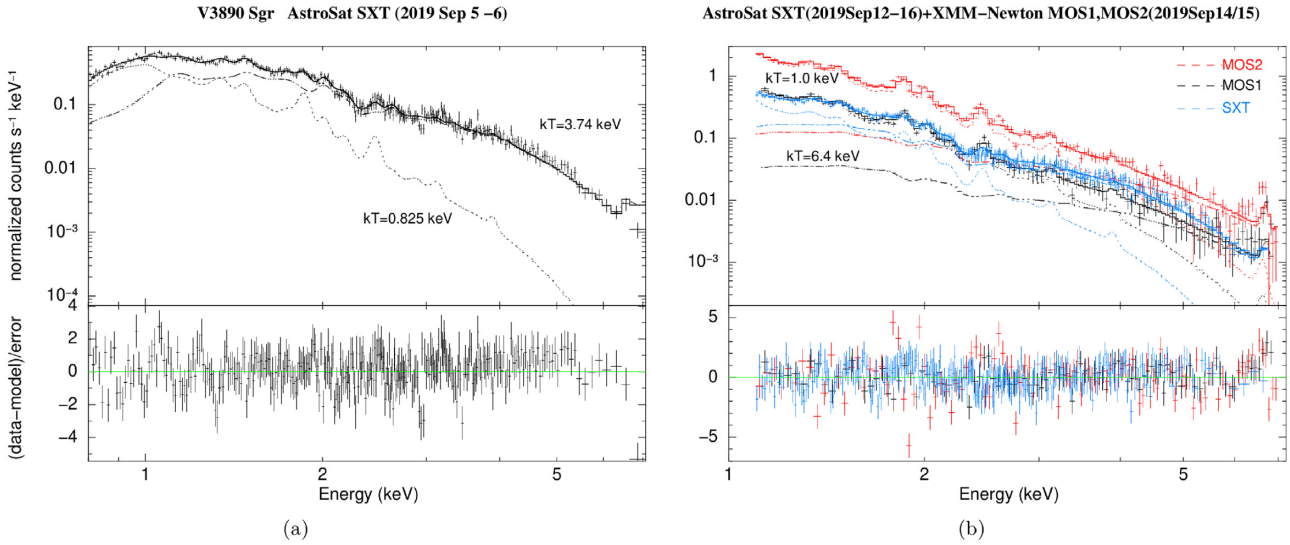

Figure 7. Merged hard X-ray spectra for S1 observation (left-hand panel) and S2 observation along with the MOS1+MOS2 observation (right-hand panel). The spectra shown are for the energy range 0.8–7.0 keV for S1, and 1.1–7.0 keV for S2, MOS1 and MOS2, for reasons as explained in the text. Best-fitting models consisting of two temperature optically thin plasmas (Model 1 for S1; Model 3 for S2 + MOS1 + MOS2) are shown as histograms. Contribution of each spectral component is also shown. All data points and lines in black show MOS1 data and models, red colour shows MOS2 data and models, and blue lines show the SXT data and models.

632 km s^{-1} for the low-temperature component and $z = -0.002\,65$ and $v = 1572$ km s^{-1} for the high-temperature component, respectively. The two plasma emission components were multiplied by a common absorber model, *Tbabs* (Tuebingen–Boulder absorption model) for interstellar medium with a single free parameter $N_{\rm H}$, i.e. the equivalent neutral hydrogen column density in the line of sight to the source. We used the baseline solar elemental abundances as listed in *aspl* (Asplund et al. 2009) in XSPEC. The abundances of

Table 1. Best-fitting spectral parameters for two temperature plasma models with a common multiplicative absorber models fitted to S1 data for energies >0.8 keV. The errors and upper limits quoted are within 90 per cent confidence. Blueshift (z) and line width values have been fixed from Orio et al. (2020). Flux values quoted at the end are independent of the models.

Parameter	Value
Model 1: *Tbabs*(*bapec* + *bapec*)	
Solar abundances	
$N_{\rm H}$ (cm^{-2})	$(10.1 \pm 0.6) \times 10^{21}$
kT_1 (keV)	0.825 ± 0.024
Blueshift (z)	$-0.002\,89$
Line width (km s^{-1})	632
EM$_1$ (cm^3)	5.9×10^{57}
kT_2 (keV)	3.74 ± 0.21
Blueshift (z)	$-0.002\,65$
Line width (km s^{-1})	1572
EM$_2$ (cm^3)	1.06×10^{58}
χ^2_ν/DOF	1.22/303
Model 2: *Tbabs*(*bapec* + *bapec*)	
Variable abundances	
$Z/Z_\odot$	0.83 ± 0.13
$N_{\rm H}$ (cm^{-2})	$(9.8 \pm 0.7) \times 10^{21}$
kT_1 (keV)	$0.83\ ^{+0.07}_{-0.02}$
EM$_1$ (cm^3)	6.75×10^{57}
kT_2 (keV)	$3.77\ ^{+0.25}_{-0.22}$
EM$_2$ (cm^3)	1.10×10^{58}
χ^2_ν/DOF	1.207/302
Model 3: *Tbabs*(*bvapec* + *bvapec*)	
Variable abundances from table 2 of Orio et al. (2020)	
$N_{\rm H}$ (cm^{-2})	$(8.11 \pm 0.5) \times 10^{21}$
kT_1 (keV)	0.82 ± 0.22
EM$_1$ (cm^3)	3.5×10^{55}
kT_2 (keV)	$3.47^{+0.17}_{-0.14}$
EM$_2$ (cm^3)	9.8×10^{57}
χ^2_ν/DOF	1.325/303
Flux$_{0.8–7.1\,\rm keV}$ (erg cm^{-2} s^{-1})	5.1×10^{-11}

all the elements in the plasma component were tied together to vary as a single parameter with respect to the solar values. The best-fitting parameters, viz. the column density, the temperatures, and the emission measures (EMs) of the plasma components (and their abundances), were obtained by using the χ^2 minimization technique as used in the XSPEC, and are given in Table 1 along with their 90 per cent confidence errors. We first tried the solar abundance values by freezing the common abundance parameter to unity (Model 1 in Table 1) and later by making it free (Model 2 in Table 1), which led to a slightly improved fit [the minimum reduced χ^2 (henceforth χ^2_ν) going down to 1.207 for 302 degrees of freedom (DOF) from 1.22 for 303 DOF] to the data (see Table 1). The best-fitting abundances in Model 2 are nearly solar for both the temperature components. The best-fitting values for two temperatures and $N_{\rm H}$ remain unchanged in both the models. The values of $N_{\rm H}$ and kT_1 are slightly lower than those obtained by Orio et al. (2020) from the *Chandra* data, while the kT_2 value is about the same considering the error bars. The best-fitting Model 1 and contributions of two spectral components are shown in the left-hand panel of Fig. 7 for the S1 spectrum.

We then fixed the elemental abundances individually for Ne, Mg, Al, Si, S, Ar, Ca, and Fe (relative to the solar values) to the values determined by Orio et al. (2020) and fitted the S1 spectrum with the *bvapec* models replacing the *bapec* models for the two temperature components, i.e. Model 3: *Tbabs*(*bvapec* + *bvapec*) in Table 1. The temperatures of two components, their normalization, and the $N_{\rm H}$ were the only free parameters here. This fit led to a slightly worse χ^2_ν of 1.325 for 303 DOF. The best-fitting value found for $N_{\rm H}$ reduced as was also found by Orio et al. (2020) to the value comparable to that reported by them with Model 3. We also found that though the temperature values in this case were nearly the same as before using *bapec*, the best-fitting EM value for the cooler component dropped significantly as was also reported by Orio et al. (2020). Given the low resolution and insufficient signal-to-noise ratio in S1 data, varying the abundances individually to differ from the fixed values, to account for 2 d difference in observations between *Chandra* and SXT, introduced too many variable parameters and did not lead to any useful determination of the abundances. We caution that the parameter values (abundances and temperatures) are only qualitative and just indicative of a possible trend as several weak lines are unresolved and can lead to wrongful estimate of continuum using global models. In addition, the atomic data base used in the analysis is continuously evolving (see the AtomDB website mentioned above). We believe that given the lower resolution in SXT vis-a-vis *Chandra* HETG, and non-simultaneity of the two observations, using *bvapec* is not necessarily warranted. We therefore have limited ourselves to using two temperature *bapec* models with variable abundances of all elements tied together, and as shown in Table 1, for all further analysis of S1 data.

We have used the *XMM–Newton* MOS1 and MOS2 data taken on day 18 after the outburst and during our long S2 observations for comparison with the merged hard X-ray spectrum obtained during the S2 observations. The SXT spectrum from the entire S2 data was used so as to have a comparable signal-to-noise in the two spectra. A major dip can be seen in the MOS1 and MOS2 data in Fig. 6 that was not covered in the SXT observation. Therefore, we extracted the spectral data from MOS1 and MOS2 before and after the dip for our comparison as described in Section 2.2. For the reasons mentioned earlier, all spectra, viz. MOS1, MOS2, and S2 used here, were for energies greater than 1.1 keV, and are shown in the right-hand panel of Fig. 7. These three spectra were fitted jointly with the same models as employed for the S1 spectrum and listed in Table 2. We first tried to fit the data with the solar abundance values by freezing the abundance parameter to unity (Model 1) and later by making it free but keeping it common for the two plasma temperature components (Model 2). We used the blueshift and velocity of 0.002 89 and 632 km s^{-1}, respectively, for both the low-temperature and high-temperature components from Orio et al. (2020). The spectral fits were found to be not very sensitive to these parameters within a range of few hundred km s^{-1} in the velocity parameters. We used a systematic uncertainty of 3 per cent in the model parameters here and in the analysis of all the S2 spectra that follow. The values of the best-fitting parameters, viz. the column density, the temperatures, the EMs of the plasma components, and the abundances, are given in Table 2. A significantly improved fit was obtained with sub-solar abundances with the χ^2_ν going down from 1.72 for 488 DOF for solar abundances (Model 1) to 1.48 for 487 DOF (Model 2). The best-fitting abundance value is nearly half the solar value and the $N_{\rm H}$ value is ∼35 per cent lower than that in the case of S1. We also fitted models where the elemental abundances of Ne, Mg, Si, S, and Fe were varied individually relative to the solar values but tied together to have the same value for the two temperature components (Model

Table 2. Best-fitting spectral parameters for two temperature plasma models with a common multiplicative absorber model fitted jointly to S2, MOS1, and MOS2 data for energies >1.1 keV. The errors and upper limits quoted are within 90 per cent confidence. The range of EM values reflects the normalization constants measured with three detectors. Blueshift ($z = -0.002\ 89$) has been fixed from Orio et al. (2020), and the line width is assumed to be nil. Flux values quoted at the end are independent of the models. A systematic error of 3 per cent was applied while fitting the data.

Parameter	Value
Model 1: *Tbabs*(*bapec* + *bapec*)	
Solar abundances	
$N_{\rm H}$ (cm^{-2})	$(6.5 \pm 0.4) \times 10^{21}$
kT_1 (keV)	0.96 ± 0.02
EM$_1$ (cm^3)	$(4.3–9.3) \times 10^{57}$
kT_2 (keV)	$4.9\ ^{+0.6}_{-0.5}$
EM$_2$ (cm^3)	$(1.2–5.3) \times 10^{57}$
χ^2_ν/DOF	1.72/488
Model 2: *Tbabs*(*bapec* + *bapec*)	
Variable abundances	
$Z/Z_\odot$	$0.47\ ^{+0.060}_{-0.054}$
$N_{\rm H}$ (cm^{-2})	$(6.0 \pm 0.5) \times 10^{21}$
kT_1 (keV)	0.95 ± 0.025
EM$_1$ (cm^3)	$(0.7–1.5) \times 10^{58}$
kT_2 (keV)	$5.7\ ^{+1.2}_{-0.7}$
EM$_2$ (cm^3)	$(1.1–5.2) \times 10^{57}$
χ^2_ν/DOF	1.48/487
Model 3: *Tbabs*(*bvapec* + *bvapec*)	
Variable abundances	
Ne/Ne$_\odot$	$2.2^{+1.1}_{-0.9}$
Mg/Mg$_\odot$	$0.45^{+0.09}_{-0.08}$
Si/Si$_\odot$	$0.64^{+0.09}_{-0.08}$
S/S$_\odot$	$0.64^{+0.12}_{-0.11}$
Fe/Fe$_\odot$	$0.46^{+0.15}_{-0.13}$
$N_{\rm H}$ (cm^{-2})	$(5.0 \pm 1.5) \times 10^{21}$
kT_1 (keV)	1.0 ± 0.04
EM$_1$ (cm^3)	$(0.6–1.1) \times 10^{58}$
kT_2 (keV)	$6.4^{+1.8}_{-1.1}$
EM$_2$ (cm^3)	$(0.9–4.6) \times 10^{57}$
χ^2_ν/DOF	1.40/483
Flux$_{\rm SXT:\ 1.1–7.1\ keV}$ (erg cm^{-2} s^{-1})	3.0×10^{-11}
Flux$_{\rm MOS1:\ 1.1–7.1\ keV}$ (erg cm^{-2} s^{-1})	2.4×10^{-11}
Flux$_{\rm MOS2:\ 1.1–7.1\ keV}$ (erg cm^{-2} s^{-1})	1.6×10^{-11}

3 in Table 2). The best-fitting parameter values obtained from a joint fit with this model to SXT S2, MOS1, and MOS2 spectra are listed in Table 2. A further improvement is seen in the best fit (χ^2_ν of 1.40 for 483 DOF) with the abundances of Mg, Si, S, and Fe being significantly sub-solar, while the abundance of Ne is indicated to lie in the range of 1.3–3.3 times solar. The Model 3 spectra are shown in the right-hand panel of Fig. 7 for a joint fit to the S2 + MOS1 + MOS2 spectra.

Using the models derived from fitting the non-variable hard X-ray component, we then proceeded to model the highly variable low-energy component of the spectra. We used Model 1 in Table 1 for the S1 data and Model 3 in Table 2 for the S2 data, for modelling the high-energy part of the spectra and added an additional component for the low-energy part, as explained below.

3.2.1 *Low-energy spectral evolution*

We modelled the spectra over the full energy range (0.3–7.1 keV) obtained for the duration of individual orbits (28 in case of S1 and 51 for S2) of the *AstroSat* SXT. As mentioned already, these spectra have useful exposure times ranging from ∼300 to ∼3000 s (most common value being ∼1700 s), and thus have low signal-to-noise ratio per energy channel. Before the appearance of the SSS phase in the spectra (for the first 8.5 d after the outburst in this case), Model 1 used in Table 1 was sufficient to get a good a fit, as expected. After the appearance of the SSS phase, however, an additional blackbody component to represent the WD atmospheric continuum was required to be added. All the spectra from the S1 observations after the day 8.5 could be well fitted by model: *Tbabs*(*bapec* + *bapec* + *bbody*) with a blackbody temperature in the range of 40–50 eV and an absorber column density, $N_{\rm H}$, of $(1.0 \pm 0.1) \times 10^{22}$ cm^{-2} for the continuum, while keeping the parameters of two *bapec* components fixed to the values given in Table 1 for Model 1 with solar abundances. Adding just a blackbody component to the spectra taken during the S2 observations, however, failed to give an acceptable χ^2_ν <2.0. Very strong residuals were observed centred in the 0.5–0.6 keV energy band, corresponding to a hump seen in the very soft part of the spectra shown in Fig. 6. The addition of a very high amplitude Gaussian with best-fitting width of 0.09 ± 0.01 keV brought the χ^2_ν down to an acceptable range of 0.9–1.5. The Gaussian could plausibly be explained as due to unresolved lines arising from the O VII triplet (0.574, 0.561, 0.569 keV), N VII (0.50 keV), and/or O VIII (0.654, 0.0653 keV) in an additional thin thermal plasma component of low temperature in the range of 0.17–0.27 keV. Replacing the line component and/or the blackbody with a plasma component, however, did not work to improve χ^2_ν and the residuals between 0.5 and 0.6 keV persisted. Besides, the supersoft emission originates from the photosphere around the WD and is thus poorly represented by an optically thin thermal plasma emission model or a blackbody. We therefore replaced the blackbody by atmospheric models for WDs provided by Tübingen NLTE Model-Atmosphere Package (TMAP).[6] The models given in TMAP calculate emission from stellar atmospheres in spherical or plane-parallel geometry in hydrostatic and radiative equilibrium while allowing for departures from local thermodynamic equilibrium (LTE) for the population of atomic levels (Rauch 1997, 2003; Rauch & Deetjan 2003). These models have been used to explain the SSS sources associated with novae, e.g. V4743 Sgr (Rauch et al. 2010). These models are available as tables that can be used in the XSPEC corresponding to a series of abundance values for the hot WD atmospheres,[7] and give fluxes for grids of effective temperatures ranging from 0.45 to 1.05 MK, in steps of 0.04 MK. The fluxes given are calculated for model series 003, 004, 005, 0,006, 0.007, 0.008, 0.009, 0.010, and 0.011 corresponding to different sets of abundance ratios. The abundance ratios used in different series vary principally for C and N elements, with decreasing depletion for C and decreasing overabundance of N with respect to solar values, going from model series 003 to 011. The surface gravity, $\log g$, is assumed to be 9. The abundance ratios of other elements are nearly constant in these models. These abundances encompass the values expected from the processing of accreted material in CNO cycle. We used these models for fitting the S2 data having bright SSS phase, using XSPEC and found that these models could fit the double-hump feature seen in spectra (Fig. 6) without requiring the addition of any

[6] http://astro.uni-tuebingen.de/~rauch/TMAP/TMAP.html
[7] http://astro.uni-tuebingen.de/~rauch/TMAF/flux_HHeCNONeMgSiS_gen.html

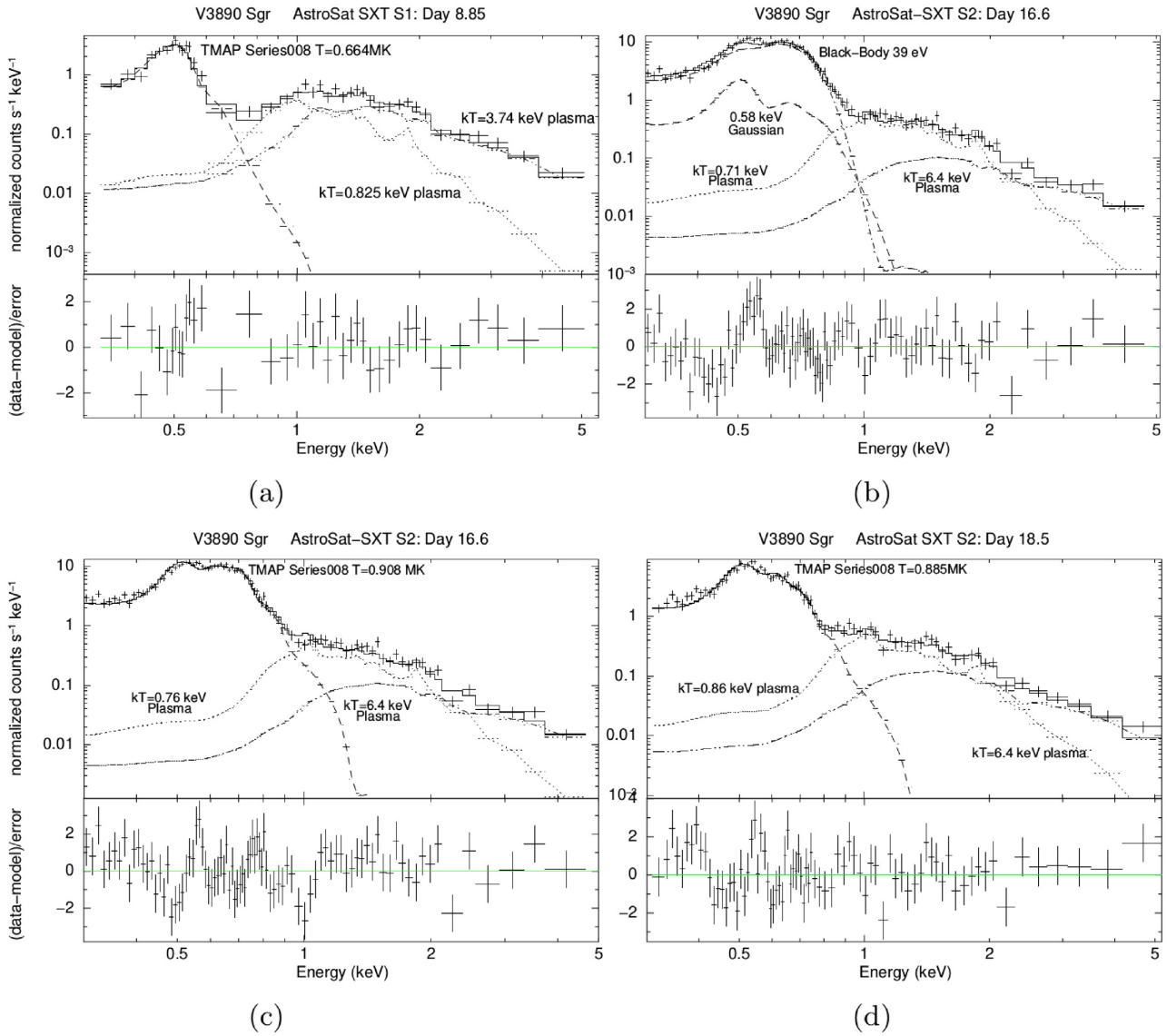

Figure 8. X-ray spectra from three epochs: one from the S1 observations on day 8.85 (panel a), and two from S2 observations: day 16.6 (panels b and c) and day 18.5 (panel d). The S1 spectrum (panel a) has been fitted with Model 1 in Table 1 plus model 008 from Tübingen NLTE Model-Atmosphere Package (see the text). S2 spectra (panels c and d) have been fitted with two temperature *bvapec* models with non-solar abundances (Model 3 in Table 2) plus model 008 from Tübingen NLTE Model-Atmosphere Package. Spectrum in panel (b) for day 16.6 shows the fit with a blackbody and a Gaussian line in addition to two plasma components for comparison with the fit shown in panel (c). The individual contributions of all the models are shown in each figure marked with different line styles and with the name of the model and the best-fitting temperatures next to them. The residuals from the overall fit are shown in the bottom panels of each figure.

Gaussian component while using a blackbody. We tried all the model series and found that S2 data show a strong preference for TMAP model series 008. These models also provided acceptable fits to the SSS phase observed in the S1 spectra, but showed no preference for any particular series. These models were invoked as *TBabs*(*bapec* + *bapec* + *atableSSS_008_00010 − 00060.bin_0.002_9.00.fits*) in the XSPEC. Examples of fits with the TMAP model to the S1 and S2 data are shown in Fig. 8 in panels (a), (c), and (d). Panel (b) in this figure shows the fit with a blackbody and a Gaussian line in addition to two plasma components for comparison with the TMAP model (panel c).

Finally, we fitted all S1 spectra with model: *TBabs*(*bapec* + *bapec* + *atableSSS_008_00010 − 00060.bin_0.002_9.00.fits*), using the temperatures, solar abundances, line broadening, line shift, and the normalization of both the plasma components, *bapec*, obtained from fitting the high-energy spectra shown in Fig. 7 frozen to the values listed in Table 1 (Model 1) as they represented the non-variable hard X-ray component. The only free parameters were $N_{\rm H}$, temperature, and normalization of the TMAP model component. The best-fitting values of $N_{\rm H}$ and temperature of the TMAP (with their 90 per cent confidence error bars), and the X-ray intensity (after absorption) in the 0.3–1.0 and 1.0–10.0 keV energy bands are plotted in Fig. 9. The $N_{\rm H}$ values vary in the range of (0.9–1.2) $\times$ 10^{22} cm^{-2} with an average value of (1.03$\pm$0.03) $\times$ 10^{22} cm^{-2}. The contribution from a TMAP model first becomes significant only on $\sim$day 8.6 after the outburst, disappearing thereafter until day 8.75, reappearing briefly on day 8.8, and disappearing again before coming on permanently from day 8.85, consistent with the data plotted in Fig. 5. The normalization of the WD atmosphere component during the act of disappearance is at least 100 times lower than that during its

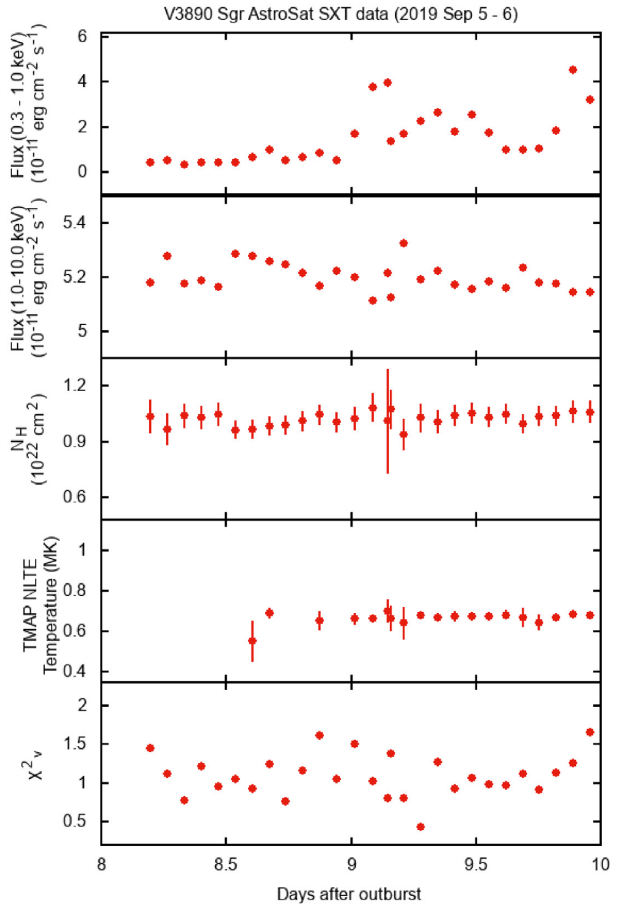

Figure 9. Spectral parameters obtained from the analysis of orbit-wise time-resolved X-ray spectra during the observation S1 shown as a function of time in days after the outbursts. The errors plotted on the parameter values are within 90 per cent confidence. The missing data points in the panel for TMAP NLTE temperature correspond to the epochs for which the SSS phase was missing or ∼100 times lower than that at the other epochs for which the errors have been determined (see also Fig. 5).

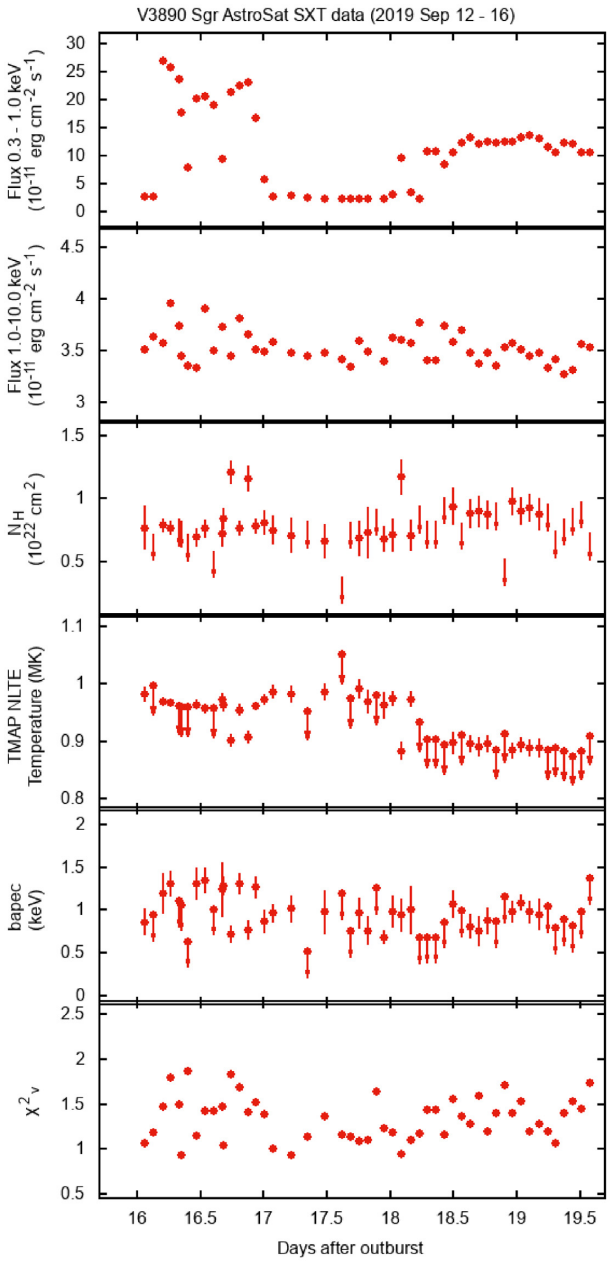

Figure 10. Spectral parameters obtained from the analysis of the time-resolved X-ray spectra during the observation S2. The errors plotted are within 90 per cent confidence. Upper limits are plotted for the epochs when the SSS phase has a very low flux.

appearance. The temperature of the TMAP component during the SSS phase of S1 observations is observed to have an average value of 0.66 ± 0.03 MK.

Spectra from the S2 observations were also fitted with *TBabs*(*bapec* + *bapec* + *atableSSS_008_00010 − 00060.bin_0.002_9.00.fits*). However, since there is a considerable overlap at the boundary between the low-temperature *bapec* component and the TMAP model (Figs 8 and 6), the temperature and the normalization of this *bapec* component were allowed to vary freely along with the temperature and normalization of the TMAP model component to get a good fit. The $N_{\rm H}$ was allowed to vary as before. Temperature of the high-temperature *bapec* component and its normalization along with the non-solar abundances, and line shift of the plasma components, obtained from fitting the high-energy spectra shown in Fig. 7, were frozen to the values shown in Table 2 (Model 3) as they represented the non-variable hard X-ray component. The best-fitting values of the free parameters with their 90 per cent confidence error bars, and X-ray intensity (absorbed) in the 0.3–1.0 and 1.0–10.0 keV energy bands for the S2 observation are shown plotted in Fig. 10. We find that even during the epochs of very low SSS flux, the presence of both a TMAP model and the thin plasma component was required to obtain a good fit even though their temperatures could not be constrained. The column density of the line-of-sight absorber also could not be constrained well during these epochs. These points are shown as upper limits in Fig. 10. The best-fitting $N_{\rm H}$ values show a lot of dispersion, ranging from 0.4×10^{22} to 1.2×10^{22} cm^{-2} with a median value of 0.8×10^{22} cm^{-2}. The column density does not seem to show any trend of being associated with the absence or presence of the SSS phase. The temperatures of the low-temperature plasma component are clustered around the average value of 1 ± 0.2 keV, similar to the 1 keV value obtained from the hard X-ray spectra shown in Fig. 7(b) and Table 2. The temperature of the TMAP model shows an average value of 0.97 ± 0.03 MK, before day 18.2, declining to 0.89 ± 0.03 MK thereafter, with both the values

being considerably higher than the value obtained during the S1 observations.

4 DISCUSSION

(i) The two dense monitoring observations of the third recorded outburst of V3890 Sgr in X-rays with *AstroSat* have added useful data for understanding the behaviour of RNe during their eruptions. The X-ray spectra recorded in these observations show an enhancement in the flux below 0.8 keV around day 8.57 since outburst discovery, almost coincident with the beginning of the SSS phase on day 8.36 (Page et al. 2019a). As shown in Fig. 1, the SSS phase peaked during days 15–20 and ended on day 26.18 (Page et al. 2019b). The duration of SSS phase can be as long as a decade (e.g. V723 Cas; Ness et al. 2008) and as short as a few days (e.g. V745 Sco; Page et al. 2015). The mass of the WD is the main factor determining the duration of the SSS phase, with WDs with low mass having a longer duration compared to the more massive WDs (Orio 2008). Short-duration SSS phase has been observed in other RNe such as U Sco, M31N 2008-12a (Henze et al. 2018), V745 Sco, and RS Oph. The SSS phase in V745 Sco was detected around 4 d since outburst, and lasted for only ∼2 d, making it the earliest switch-on and shortest duration SSS ever detected (Page et al. 2015). The early switch-on is attributed to a combination of low ejected mass with high velocity, high effective temperature, and a high-mass WD (>1.3 $M_\odot$) (Page et al. 2015). RS Oph, on the other hand, showed the SSS onset on day 26 during the 2006 outburst, with the SSS phase lasting for ∼60 d (Bode et al. 2006; Osborne et al. 2011). A high-mass WD is also inferred for RS Oph (Osborne et al. 2011). The early onset of the SSS phase in V3890 Sgr indicates a high-mass WD in this RN too. Adopting the relation between the SSS turn-on and ejected mass by Shore (2008), $M_{ej} \sim 2 \times 10^{-6}$ $M_\odot$ is estimated. An accretion rate of $\sim 2 \times 10^{-7}$ $M_\odot$ yr^{-1} is estimated using the relations in Page et al. (2015) and Henze et al. (2014), and by adopting super-Eddington luminosity as suggested by Gonzalez-Riestra (1992) for the 1990 outburst. These estimates indicate that not all the accreted material is ejected during the nova outburst. Theoretical models show that WDs of mass 1.35 $M_\odot$ increase in mass irrespective of the accretion rate and could eventually reach the Chandrasekhar limit (Starrfield et al. 2020).

(ii) A detailed spectral analysis of our two long observations (day 8.1–9.9, and day 15.9–19.6 after outburst) has revealed at least two plasma components dominating the emission at energies above 1 keV, while an additional soft component dominates at lower energies. The average X-ray spectrum above 1 keV taken during our first set of observations (S1) is consistent with *Chandra* high-resolution X-ray spectra taken 2 d before the start of our observations. The temperatures of ∼0.8 and ∼4.0 keV for the two plasma components and the absorbing column density value of $\sim 10^{22}$ cm^{-2} derived from global fits are similar to the values reported based on *Chandra* observations based on similar analysis. The EM values of the plasma components here (see Table 1) are only slightly lower than those given in table 2 of Orio et al. (2020). In our case, the EM values are in the range (0.6–0.7) $\times 10^{58}$ cm^{-3} for the cool ($kT = 0.8$ keV) component and $\sim 1.1 \times 10^{58}$ cm^{-3} for the hot ($kT \sim 4.0$ keV) plasma component (Table 1). When the variable abundance model *bvapec* is used, the EM for the cool component goes down considerably to 3.5×10^{55} cm^{-3}, similar to the trend seen in table 2 of Orio et al. (2020). These values, though model dependent, can be used to get a rough idea of the electron density in the plasma if the size of the region responsible for the plasma components is known. If the plasma components are assumed to be coming from a region of radius 1 au, then the electron density in the plasma would range from (7–9) $\times 10^8$ cm^{-3}. This is somewhat lower than the typical values derived from optical spectra of other novae at early phases. For example, Neff, Smith & Ketelsen (1978) estimated a value 1.7×10^{10} cm^{-3} on the ninth day after the outburst for V1500 Cyg. Further, the models by Moore & Bildsten (2012), Orlando, Drake & Laming (2009), and Orlando, Drake & Miceli (2017) indicate post-shock electron density in the range of 10^9–10^{10} cm^{-3} for the post-shock material in symbiotic RNe assuming a spherically symmetric expansion of the plasma. We will mention, however, that in the *Chandra* observation on day 6, Orio et al. (2020) found spectral diagnostics suggesting the possibility of a very dense, localized and probably clumpy emission region, occupying only a tiny part of the 1-au radius sphere. In this case, the X-ray spectrum at that epoch would have probably been emitted very close to the red giant, with electron density as high as 10^{13} cm^{-3}.

(iii) We have also analysed the MOS1 and MOS2 data obtained from *XMM–Newton* observations on an epoch during our second set of observations, S2, and carried out a joint spectral fit to the high-energy (>1.1 keV) MOS1 + MOS2 + SXT data in the same energy band. The SXT data were, however, merged for the entire duration of the S2 observations to have comparable statistics in this steady high-energy part of the spectrum. We find that the fluxes in this energy range of 1.1–7.1 keV agree to within 20 per cent for the SXT and MOS1 (MOS2 data taken in a different mode show a much lower flux), while all the spectral parameters (see Table 2) are the same for all three spectra. A comparison with the best-fitting parameters derived from the S1 observations shows that: the temperatures of the thin equilibrium plasma components are somewhat higher, the column density is about 30 per cent lower, and the elemental abundances are significantly lower (about half) with respect to solar. The best-fitting N_H values, however, show a lot of dispersion for the duration of the S2 observation with a median value of 0.8×10^{22} cm^{-2}. The trend for decreasing column density has also been reported by Page et al. (2019b), who saw a decrease of column density from 3.4×10^{22} cm^{-2} on day 8.1 to $0.17^{+0.5}_{-0.6} \times 10^{22}$ cm^{-2} on day 28.8 after the outburst. The exact values, however, are dependent on the abundance model and abundance table used in the analysis. Decrease in the column density was also detected in both RS Oph and V745 Sco, with ($N_H \propto t^{-\alpha}$), where α was found to be ∼0.5 in RS Oph, while it was somewhat steeper with $\alpha = 0.76$ in V745 Sco (Bode et al. 2006; Page et al. 2015). This could be the result of complex mixing processes of nova ejecta and red giant wind as the nova evolves. In fact, model calculations by Orlando et al. (2009) indicate that different regions of plasma at different temperatures could also have a different mixture of elements, and quite different abundances.

(iv) The sum of the two plasma components is steady in two SXT observations while the source intensity varies erratically at energies below 1 keV. A soft component dominates the spectra from ∼8.57 d onwards, and is responsible for all the variations in the intensity observed after that day. The soft component below <1 keV could be modelled either using TMAP models or a blackbody for both the S2 spectra and S1 spectra (after the appearance of the SSS phase). The addition of a blackbody alone was not sufficient to fit the spectra from S2 observations, however, and required the addition of a narrow Gaussian component in the energy range of 0.5–0.65 keV. The Gaussian component could likely originate due to transitions of the O VII (0.574, 0.561, 0.569 keV), N VII (0.50 keV) from a plasma at a temperature of 0.172 keV, and O VIII (0.654, 0.653 keV) from a plasma of temperature 0.272 keV. The TMAP models, however, provided good fit to S2 spectra without needing any additional Gaussian component, and also fitted the S1 spectra

quite well. We therefore studied the evolution of the soft component using only the TMAP models. The best-fitting TMAP models show a preference for model series 008, which shows a lesser depletion of C and N in CNO burning as compared to the depletion in model 003 that was used by Osborne et al. (2011) to study the SSS phase of RS Oph. These abundance values also impact the determination of the mass of the WD as shown by Starrfield et al. (2020). The temperature of the TMAP models shows the presence of a very hot photosphere with temperature increasing from 0.68 MK to an average of 0.94 MK from S1 observations to S2 observations, with an indication of slight cooling from a peak of 1.0 MK to <0.9 MK after day 18.2. The temperature of the low-temperature plasma component also seems to have increased from 0.83 keV in S1 data to ∼1.0 keV in S2 data. If the low-temperature components disappear during days subsequent to the disappearance of the blackbody as reported in *Swift* observations nearly 30 d after the eruption, then it would indicate low cooling time due to high density in the low-temperature components.

(v) The complete disappearance of SSS phase seen as very low flux lasting for 1 d (16.8–17.8 d after the outburst) during the S2 observations, and observed as a sharp dip a little later with *XMM–Newton* could be the result of a sudden new outflow of matter that is completely opaque to X-rays but does not fill the space, thereby reducing the flux but not the spectral shape or $N_{\rm H}$ or patchy absorption by clumpy ejecta. It does not appear to be associated with increased overall absorption, although the determination of the $N_{\rm H}$ is complicated by low flux and poor signal-to-noise ratio during some of these epochs. In fact, the $N_{\rm H}$ values show a wide range after the addition of TMAP models, as compared with a low value obtained from the average high-energy spectra from S2 observations, thus indicating the complexity of ejecta, chemical composition, and mixing with accretion from symbiotic giant star.

The reasons for the rapid variability on time-scales of several minutes to hours observed in the intensity of very soft X-rays (0.3–1.0 keV) are not clear, however.

(vi) The complex interplay of blackbody like emission and coronal lines versus TMAP models requires monitoring with high spectral resolution. For example, coronal lines have been reported from high-resolution *Chandra* observations of the SSS Cal87 in the Large Magellanic Cloud (Ness et al. 2012, 2013). The presence of coronal line emission due to O VI has been seen in the optical spectra from day 12 onwards by Pavana et al. (2019b), along with the other coronal lines due to [Fe XIV], [Fe VII], [Fe X], and [Fe XI] during the active SSS phase. Our optical data (M. Pavana et al., in preparation) also indicate that the optical coronal emission lines originate in a region very close to the red giant.

5 CONCLUSIONS

The two long extended observations with *AstroSat* cover the nova evolution with the densest possible monitoring from a low-Earth orbit. It demonstrates the fast evolution of SSS emission including a rapid first appearance on day 8.57 after the outburst. The subsequent evolution remains highly variable, demonstrating the importance of long-term high-cadence monitoring. A complete vanishing of the supersoft emission during days 8.6–8.9 followed by another extremely low flux state lasting for 1 d (day 16.8–17.8) has also been detected. The abruptness with which SSS emission brightens and fades (or disappears) poses a challenge to evolutionary models of the ejecta, a discussion on which is beyond the scope of this work. Long-duration continuous observations with higher resolution instruments of future outbursts in such novae are needed to get a better understanding of the evolution of such systems.

ACKNOWLEDGEMENTS

We are thankful to Kim Page of the University of Leicester, UK, for providing us with data from observations with *Swift* for our Fig. 1. We thank the Indian Space Research Organisation for scheduling the observations within a short period of time and the Indian Space Science Data Centre (ISSDC) for making the data available. This work has been performed utilizing the calibration data bases and auxiliary analysis tools developed, maintained, and distributed by *AstroSat*-SXT team with members from various institutions in India and abroad and the SXT Payload Operation Center (POC) at the Tata Institute of Fundamental Research (TIFR), Mumbai for the pipeline reduction. The work has also made use of software, and/or web tools obtained from NASA's High Energy Astrophysics Science Archive Research Center (HEASARC), a service of the Goddard Space Flight Center and the Smithsonian Astrophysical Observatory. We thank the *XMM–Newton* team for carrying out the observations. *XMM–Newton* is an ESA (European Space Agency) science mission with instruments and contributions directly funded by ESA Member States and NASA (National Aeronautics and Space Administration). We thank an anonymous referee for the comments that substantially improved the presentation of our analysis and results.

DATA AVAILABILITY

Data from observations used in this paper are publicly available at the *AstroSat* archives of ISRO maintained by the ISSDC.[8] Data from *XMM–Newton* observations are also public and can be retrieved via *XMM–Newton* Science Archive.[9]

REFERENCES

Anupama G. C., 2013, in Di Stefano R., Orio M., Moe M., eds. Proc. IAU Symp. 281, Binary Paths to Type Ia Supernovae Explosions. Kluwer, Dordrecht, p. 154
Anupama G. C., Kamath U., 2012, Bull. Astron. Soc. India, 40, 161
Anupama G. C., Mikolajewska J., 1998, A&A, 344, 177
Anupama G. C., Sethi S., 1994, MNRAS, 269, 105
Arnaud K. A., 1996, in Jacoby G., Barnes J., eds, ASP Conf. Ser. Vol. 101, Astronomical Data Analysis Software and Systems V. Astron. Soc. Pac., San Francisco, p. 17
Asplund M., Grevesse N., Sauval A. J., Scott P., 2009, ARA&A, 47, 481
Bailer-Jones C. A. L., Rybizki J., Fouesneau M., Mantelet G., Andrae R., 2018, AJ, 156, 58
Beardmore A. P., Osborne J. P., Page K. L., Ness J. U., Orio M., Drake J. J., 2019, Astron. Telegram, 13104, 1
Bode M. F. et al., 2006, ApJ, 652, 629
Burrows D. N. et al., 2005, Space Sci. Rev., 120, 165
Buson S., Jean P., Cheung C. C., 2019, Astron. Telegram, 13114, 1
Duerbeck H. W., 1987, Space Sci. Rev., 45, 1
Fullerton A. W., Massa D. L., Prinja R. K., Owocki S. P., Cranmer S. R., 1997, A&A, 327, 699
Gonzalez-Riestra R., 1992, A&A, 265, 71
Henze M. et al., 2014, A&A, 563, A2
Henze M., Darnley M. J., Shafter A. W., Kafka S., Kato M., Williams S. C., 2018, Astron. Telegram, 12207, 1
Hoegbom J. A., 1974, A&AS, 15, 417
Jansen F. et al., 2001, A&A, 365, L1
Jones A., Pearce A., 1990, IAU Circ., 5004, 3

[8] https://astrobrowse.issdc.gov.in/astro_archive/archive/Home.jsp
[9] http://nxsa.esac.esa.int/nxsa-web/#search

Krautter J., 2008, in Bode M. F., Evans A., eds, Classical Novae, 2nd edn, Cambridge Astrophysics Series 43. Cambridge Univ. Press, Cambridge, p. 232
Liller W., 1990, IAU Circ., 5127, 1
Moore K., Bildsten L., 2012, ApJ, 761, 182
Mukai K., 2015, Acta Polytechnica CTU Proceedings, 2, 246
Munari U., Walter F. M., 2019, Astron. Telegram, 13069, 1
Neff J. S., Smith V. V., Ketelsen D. A., 1978, ApJS, 38, 89
Ness J. U., 2012, Bull. Astron. Soc. India, 40, 353
Ness J. U., Schwarz G., Starrfield S., Osborne J. P., Page K. L., Beardmore A. P., Wagner R. M., Woodward C. E., 2008, AJ, 135, 1328
Ness J. U. et al., 2012, ApJ, 745, 43
Ness J. U. et al., 2013, A&A, 559A, 50
Ness J. U. et al., 2019, Astron. Telegram, 13124, 1
Nyamai M. M., Woudt P. A., Ribeiro V. A. R. M., Chomiuk L., 2019, Astron. Telegram, 3089, 1
Orio M., 2008, Bull. Astron. Soc. India, 40, 333
Orio M., 2015, Proc. Sci., Recurrent Novae in the Local Group. SISSA, Trieste, PoS#64
Orio M. et al., 2020, ApJ, 895, 80
Orlando S., Drake J. J., Laming J. M., 2009, A&A, 493, 1049
Orlando S., Drake J. J., Miceli M., 2017, MNRAS, 464, 5003
Osborne J. P. et al., 2011, ApJ, 727, 124
Page K. L. et al., 2015, MNRAS, 454, 3108
Page K. L., Beardmore A. P., Osborne J. P., Orio M., Sokolovsky K. V., Darnley M. J., 2019a, Astron. Telegram, 13084, 1
Page K. L. et al., 2019b, Astron. Telegram, 13137, 1
Pavana M., Anupama G. C., Pramod Kumar S., 2019a, Astron. Telegram, 13060, 1
Pavana M., Roy N., Anupama G. C., Singh K. P., Girish V., 2019b, Astron. Telegram, 13092, 1
Pereira A., 2019, [VSNET-Alert 23505] V3890 Sgr Outburst (Alfredo Pereira, Carnaxide, Portugal)
Rauch T., 1997, A&A, 320, 237
Rauch T., 2003, A&A, 403, 709
Rauch T., Deetjen J. L., 2003, in Hubeny I., Mihalas D., Werner K., eds, ASP Conf. Ser. Vol. 288, Stellar Atmosphere Modeling. Astron. Soc. Pac., San Francisco, p. 103
Rauch T., Orio M., Gonzales-Riestra R., Nelson T., Still M., Werner K., Wilms J., 2010, ApJ, 717, 363
Roberts D. H., Lehar J., Dreher J. W., 1987, AJ, 93, 968
Schaefer B., 2009, ApJ, 697, 721
Schaefer B., 2010, ApJS, 187, 275
Schaefer B. E., 2018, MNRAS, 481, 303
Shore S. N., 2008, in Bode M., Evans A., eds, *Classical Novae, 2nd edn,* Cambridge Astrophysics Series 43. Cambridge Univ. Press, Cambridge, p. 194
Singh K. P. et al., 2014, in Takahashi T., den Herder J.-W. A., Bautz M., eds, Proc. SPIE Conf. Ser. Vol. 9144, Space Telescopes and Instrumentation 2014: Ultraviolet to Gamma Ray. SPIE, Bellingham, p. 91441S
Singh K. P. et al., 2016, in den Herder J.-W. A., Takahashi T., Bautz M., eds, Proc. SPIE Conf. Ser. Vol. 9905, Space Telescopes and Instrumentation 2016: Ultraviolet to Gamma Ray. SPIE, Bellingham, p. 99051E
Singh K. P. et al., 2017, J. Astrophys. Astron., 38, 29
Singh K. P., Girish V., Anupama G. C., Pavana M., 2019a, Astron. Telegram, 13102, 1
Singh K. P., Girish V., Anupama G. C., Pavana M., 2019b, Astron. Telegram, 13145, 1
Sokolovsky K. V. et al., 2019, Astron. Telegram, 13050, 1
Starrfield S., Iliadis C., Timmes F. X., Hix W. R., Arnett W. D., Meakin C., Sparks W. M., 2012, Bull. Astron. Soc. India, 40, 419
Starrfield S., Bose M., Iliadis C., Hix W. R., Woodward C. E., Wagner R. M., 2020, preprint (arXiv:2006.01827v1)
Strader J. et al., 2019, Astron. Telegram, 13047, 1

This paper has been typeset from a TEX/LATEX file prepared by the author.